Wi2DMeasure: WiFi-based 2D Object Size Measurement

Xuanzhi Wang[1], Junzhe Wang[1], Kai Niu[2], Jie Xiong[3], Fusang Zhang[4], Enze Yi[1],
Anlan Yu[1], Zhiyun Yao[1], Daqing Zhang[1,5]

[1]School of Computer Science, Peking University, [2]Xiaomi Corporation, [3]Microsoft Research Asia & University of
Massachusetts Amherst, [4]Institute of Software, Chinese Academy of Sciences, [5]SAMOVAR, Telecom SudParis, IP Paris
xuanzhiwang@stu.pku.edu.cn, wjz020606@stu.pku.edu.cn, xjtunk@pku.edu.cn, jxiong@cs.umass.edu,
fusang@iscas.ac.cn, yienze_cs@pku.edu.cn, yal6040@pku.edu.cn, zhiyunyao@stu.pku.edu.cn, dqzhang@sei.pku.edu.cn

ABSTRACT

While a large range of sensing applications such as activity sensing and vital sign monitoring have been realized with WiFi sensing, using commercial WiFi devices to obtain fine-grained size information of objects remains challenging due to the narrow bandwidth of WiFi. Very recent studies attempted to measure object sizes using WiFi signals. However, these systems are still far from practical with a lot of limitations including requiring multiple transceiver pairs and can only measure one-dimensional size, hindering their real-life adoption. Also, these systems rely on Channel State Information (CSI) to work, which is only available on few commercial WiFi cards. In this work, we propose to employ a new channel data, i.e., Beamforming Feedback Information (BFI), widely available on almost all new generation WiFi cards for fine-grained size measurement. Through thoroughly analyzing the mathematical relationship between BFI and CSI, we show how to use BFI to achieve fine-grained size measurement. We propose a novel method to accurately measure the two-dimensional size of an object using a single transceiver pair by identifying the positions of singularities when the object passes through the diffraction zone of the transceiver pair. Experiment results show that Wi2DMeasure can accurately measure the two-dimensional size of objects under various conditions, achieving a small median error of only 3.7 mm.

CCS CONCEPTS

• **Human-centered computing** → **Ubiquitous computing**.

KEYWORDS

WiFi sensing, Size measurement, Diffraction zone, BFI, CSI

1 INTRODUCTION

In the last few years, wireless sensing has attracted a lot of attention from both academia and industry. Besides the conventional functions (e.g., communication), wireless signals are extensively explored for sensing purposes. Among the signals recently exploited for sensing, WiFi stands out owing to the ubiquitous deployment of WiFi infrastructure in indoor environments and the widespread availability of WiFi modules in smartphones, home appliances and IoT devices. A large range of motion-based applications have been enabled with WiFi sensing including intruder detection [23, 24, 45], trajectory tracking [25, 26, 31, 50], activity/gesture recognition [1, 12, 15, 49, 57], and vital sign monitoring [29, 32, 42, 44, 54, 56]. Besides motion sensing, WiFi signals have also been applied for material sensing such as liquid recognition leveraging fine-grained phase changes when signals propagate through the target [10, 38, 39].

While promising, we notice that very little attention has been paid to WiFi-based target size sensing. This is mainly due to the limited frequency bandwidth (e.g., 20-40 MHz) of WiFi signals and conventional imaging-based size measurement requires a large bandwidth. It can thus only be realized with large-bandwidth signals such as UWB (ultra-wideband) and mmwave signals which have a bandwidth larger than 500 MHz. While conventional LiDAR and radar can capture the shape information of a target, obtaining accurate size information is still challenging and the accuracy of size measurement is limited to a few centimeters [8]. On the other hand, target size measurement plays an important role in many real-world applications such as logistics and quality control. In logistics, size information helps save storage space efficiently. In fruit quality control, fruits are graded based on size for pricing.

Very recently, some preliminary work explored the possibility of employing WiFi signals which are narrow band for size measurement [43]. Instead of employing reflection which requires a large bandwidth, diffraction is employed for size measurement. However, the proposed system requires multiple transmitter-receiver pairs which is far from practical and can only capture the size information of one target dimension. Another critical issue associated with the proposed system is that it relies on Channel State Information (CSI) readings for sensing. Besides technical challenges, one practical issue hindering WiFi sensing from being adopted in real life is the non-availability of CSI readings on the vast majority of commodity WiFi hardware.

In this work, we address all the issues associated with the existing solution, moving WiFi-based size measurement one step forward towards real-life adoption. The proposed system exhibits the following advantages:
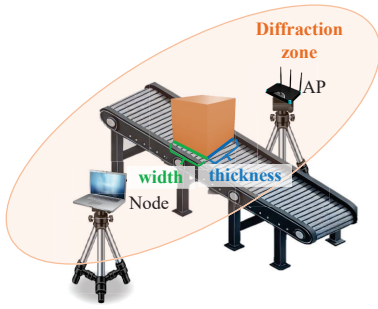
Figure 1: Two-dimensional object size measurement with one pair of WiFi transceivers.
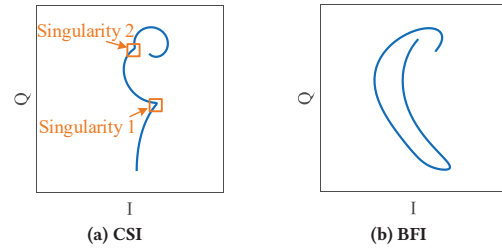

Figure 2: The ideal CSI signal exhibits two singularities when the target moves in the diffraction zone, whereas the BFI signal does not contain any singularities.

- **Universal Accessibility of BFI on Modern WiFi Devices:** Compared to CSI which is available on very few WiFi devices, BFI readings are available on almost all new-generation commodity WiFi devices. With the widespread adoption of the IEEE 802.11ac/ax WiFi standards, an increasing number of commercial WiFi devices nowadays support MU-MIMO (multi-user multiple-input multiple-output) technology. To enable MU-MIMO, Beamforming Feedback Information (BFI) is measured at the WiFi nodes and transmitted to the WiFi access point (AP). Since BFI also contains channel information, it can be used for sensing just like CSI. What makes BFI exciting is that BFI is transmitted without encryption and it can be extracted from almost all new-generation WiFi devices on the market without requiring any firmware or driver hacking. For example, BFI is supported by smartphones including iPhone, Samsung Galaxy phones, Google Pixel phones and Xiaomi phones. For access points, nine out of the top ten best sellers on Amazon support BFI [3].

- **Accurate Size Measurement with a Single Device Pair:** It requires only one pair of WiFi transceivers for size measurement. The state-of-the-art solution utilizes the number of singularity points to infer the target size [43]. This is coarse because a particular number of singularities correspond to a target size range (e.g., 4-10 cm) but not a precise size. Therefore, multiple transceiver pairs need to be employed to narrow down the range for accurate estimates. In this work, we propose to capture the fine-grained position information of the singularity points to estimate the target size which requires just one transceiver pair.

- **Two-Dimensional Size Sensing Capability:** The proposed system can capture two-dimensional size information of the target. Existing method [43] can only capture the size information of one target dimension. By leveraging multiple antennas widely available at WiFi APs nowadays, we can measure the projection of the two-dimensional target size (i.e., width and thickness in Figure 1) from slightly different angles. By smartly fusing the projection views from different angles, we can obtain the size information of two dimensions. Note that we consider the most commonly seen case that the target moves with a horizontal conveyor belt and the transceiver pair does not move. Size information of the third dimension (i.e., height) can be obtained if the conveyor belt has vertical displacement.

While promising, we encountered multiple challenges before we can turn the exciting idea into a functioning system.

- **Challenge 1:** To reduce the transmission overhead, BFI is a compressed version of CSI, containing only partial CSI information [52]. BFI essentially is a distorted version of the original CSI, rendering direct application of existing CSI-based sensing models infeasible. Take size measurement as the example. The occurrence of singularities (i.e., abrupt changes in direction) on the CSI curve as illustrated in Figure 2a is the key information utilized for size measurement. However, the BFI curve may not even contain any singularities as shown in Figure 2b. Recovering precise singularity information from the distorted BFI data for accurate size measurement presents a big challenge.

- **Challenge 2:** To reduce the BFI transmission overhead for MU-MIMO communication, BFI adopts a much lower sampling rate compared to CSI. This low sampling rate makes it difficult to extract the precise positions of the singularities which are critical for size measurement. Furthermore, compared to CSI-based method which relies on counting the number of singularity points for sensing, it is much more difficult to obtain the precise positions of the singularity points under low sampling rate and hardware noise.

- **Challenge 3:** There is no exiting model which captures the relationship between the positions of the singularities and the target size. Two-dimensional size measurement further complicates the problem because size information extracted at each antenna pair is a one-dimensional projection of the target size. The two-dimensional size information is thus superimposed in the one-dimensional projection. Even with the novel idea of leveraging multiple antenna pairs to capture multiple views of the projection, it is still non-trivial to separate and obtain precise size information of each individual dimension.

To address the first challenge, we establish the mathematical relationship between BFI and CSI. Although it is not possible to fully recover CSI using BFI, we show that BFI can be used to represent CSI ratio. Through deeply understanding the mathematical relationship, we show that CSI ratio can be represented by the trigonometric functions of BFI readings. We further prove that when two antennas are close to each other, CSI ratio and the two CSIs exhibit roughly the same singularity characteristics. When the spacing between two antennas are relatively large (e.g., 20 cm), the singularity characteristics of the CSI ratio is only similar to the CSI whose signal link is closer to the target. Thus, to fully utilize all the antennas available for sensing, the spacing between antennas needs to be taken into consideration. To deal with the second challenge,

we increase the number of samples to reduce the noise level leveraging the Law of Large Numbers [4]. Specifically, we increase the sampling rate through interpolation [35] and utilize a large number of subcarriers available at commodity WiFi hardware. To address the third challenge, we first establish the quantitative relationship between the position of the singularity and the target size for one antenna pair. A singularity occurs when the signal propagation length difference along the upper boundary and lower boundary of the target is an integer multiple of the signal wavelength. The position of the singularity is thus related to the target size, i.e., the distance between the target upper boundary and lower boundary. We thus measure the two-dimension size of the object from slightly different angles using projections obtained from different antenna pairs. As WiFi antennas are co-located, the diversity of the projections is not that big. We thus adopt the least squares method [47] to obtain the optimal values for target size estimates.

To summarize, the main contributions are as follows.

- Based on a deep understanding of the mathematical relationship between BFI and CSI, we show that although CSI is not able to be fully recovered using BFI, we can construct CSI ratio using BFI. As CSI ratio and CSI share similar sensing capabilities in a lot of scenarios, we successfully enable sensing with BFI, laying the theoretical foundation for sensing with new-generation WiFi cards.
- To achieve accurate two-dimensional size measurement of objects using just a single pair of transceivers, for the first time, we propose to use the position information of the singularity points when a target moves across the diffraction zone of the transceiver pair. We address critical inherent issues associated with BFI such as low sampling rate and high noise leveraging interpolation and the large number of subcarriers available at commodity WiFi hardware.
- We show for the first time that antenna spacing affects the characteristics of the constructed CSI ratio using BFI and propose corresponding strategies for different antenna spacing cases. To obtain accurate size estimates, we fuse the information captured at multiple antenna pairs as an optimization problem and adopt the least squares method with linear regression to obtain the final estimates.
- We implement the proposed system Wi2DMeasure on commodity WiFi hardware and show that the proposed system can measure the two-dimensional size of the target at a median error of 3.7 mm with a single transceiver pair, pushing WiFi-based size measurement one important step towards real-world adoption.

2 BACKGROUND KNOWLEDGE

Before presenting our design, we first introduce the principle of size measurement using CSI and the basics of BFI.

2.1 CSI-based Size Measurement

In WiFi transmission, CSI is used to describe the characteristics of signal propagation paths from the AP to the node. For a wireless channel with a central frequency f, the CSI of this channel at time t can be expressed as $H(f, t) = Y(f, t)/X(f, t)$, where $Y(f, t)$ and $X(f, t)$ are the frequency domain representations of the transmitted

(a) Diffraction model (b) CSI readings on the I-Q plane
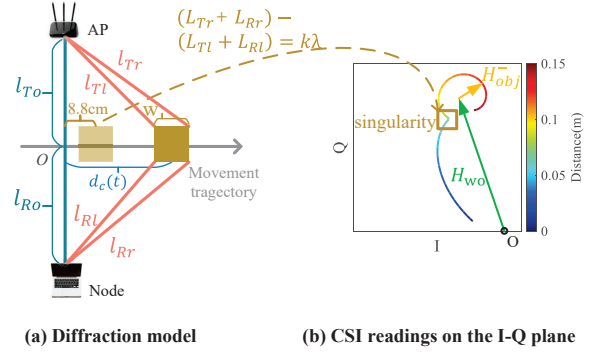
Figure 3: When the signal path difference on two sides of the object is an integer multiple of the signal wavelength, the signal curve exhibits singularities on the I-Q plane.

and received signals, respectively. When the positions of the AP and node are fixed, and an object moves through the diffraction zone as shown in Figure 3a, the received signal can be expressed as the signal without object $H_{wo}(f, t)$ minus away the signal blocked by the object $H_{obj}(f, t)$. Specifically, $H_{wo}(f, t)$ does not change over time and is the static component in the received signal, while $H_{obj}(f, t)$ varies with the object movement and is the dynamic component. Mathematically, the received signal can be expressed as:

$$H(f, t) = H_{wo} - H_{obj}(f, t)$$
$$= H_{wo} - \frac{i}{2\lambda} \int_{d_c(t) - \frac{W}{2}}^{d_c(t) + \frac{W}{2}} \frac{A}{l_T l_R} e^{-i\frac{2\pi \cdot (l_T + l_R)}{\lambda}} dx, \quad (1)$$

where λ is the signal wavelength, and A is the amplitude of the transmitted signal. H_{obj} can be obtained by integrating the signal from the left boundary of the object $d_c(t) - \frac{W}{2}$ to the right boundary of the object $d_c(t) + \frac{W}{2}$, where d_c is the vertical distance from the center of the object to the LoS path, and W is the object width. The path lengths from the integral point with vertical height x to the AP and node are $l_T = \sqrt{l_{To}^2 + x^2}$ and $l_R = \sqrt{l_{Ro}^2 + x^2}$, respectively. Here l_{To} (l_{Ro}) represents the distance from the vertical projection point (i.e., O) on the LoS to AP (node).

To further analyze signal variation patterns when the object moves across the LoS path, we visualize the signal in Equation 1 as vectors on the I-Q plane. For simplicity, we denote $-H_{obj}(f, t)$ as $H_{obj}^-(f, t)$, so the received signal is the vector addition of H_{wo} and $H_{obj}^-(f, t)$ on the I-Q plane, as shown in Figure 3b. On the I-Q plane, the diffraction signal vector $H_{obj}^-(f, t)$ rotates with respect to the static signal vector H_{wo}, leading to variations of the received signal vector $H(f, t)$.

Note that different object widths lead to different path length differences between the right boundary ($L_{Tr} + L_{Rr}$) and left boundary ($L_{Tl} + L_{Rl}$) of the object. Singularity occurs when the path length difference between the left and right boundaries of the object is an integer multiple of the wavelength λ which can be expressed as:

$$(L_{Tr} + L_{Rr}) - (L_{Tl} + L_{Rl}) = k\lambda. \quad (2)$$

As shown in Figure 3b, when the LoS distance is 1 m, an object with a width of 0.1 m produces a singularity point when it
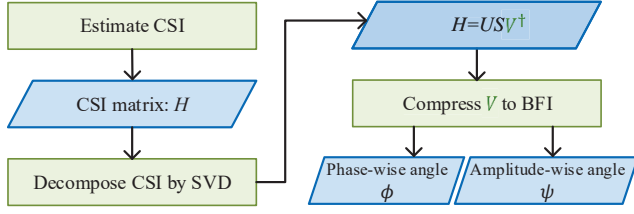
Figure 4: The sounding procedure for MU-MIMO transmissions (IEEE 802.11ac).

moves outward from the midpoint of the LoS along the perpendicular bisector. The width of the object is related to the number of singularities as the object moves along a specified trajectory.

2.2 BFI Primer

BFI is mainly used to enable MU-MIMO transmission, a key feature of the 802.11ac/ax WiFi standards. Figure 4 shows the procedure of obtaining BFI. To support MU-MIMO, the WiFi AP needs to know the channel state information between the AP and all nodes. Directly transmitting complete CSI to the AP incurs significant overhead. To reduce this overhead, the node uses Singular Value Decomposition (SVD) to decompose the measured CSI. Specifically, SVD decomposes the CSI matrix H into three matrices: $H = USV^{\Gamma}$, where matrices U and S represent the information at the node and the channel gain, respectively, and matrix V contains the most critical beamforming feedback information for the AP. Γ denotes the conjugate transpose operation. To further reduce the communication overhead, matrix V is compressed into two angle information ϕ and ψ (i.e., BFI), which are subsequently sent to the AP for MU-MIMO transmission.

3 SYSTEM OVERVIEW OF WI2DMEASURE

Figure 5 presents an overview of the system, which consists of four modules: data acquisition, signal construction, singularity extraction, and 2D size measurement.

- **Data acquisition:** To collect BFI readings, we employ a sniffer to monitor the beamforming feedback packets using Wireshark. To support MU-MIMO, the AP is equipped with multiple antennas.
- **Signal construction:** BFI is a compressed version of CSI. Although CSI is not able to be fully recovered using BFI, CSI ratio which possesses similar sensing capability as CSI can be reconstructed from BFI.
- **Singularity extraction:** Since the sampling rate of BFI data is only tens of hertz, we employ linear interpolation to increase the number of samples. We further leverage the law of large numbers to combine BFI data from multiple subcarriers to reduce the noise. Using the up-sampled and noise-reduced signal samples, we can accurately extract the positions of singularities for fine-grained object size measurement.
- **2D size measurement:** For each antenna pair, we calculate the object's size projection using the singularity positions. By combining the measurement results of multiple antenna pairs, we obtain the accurate width and thickness of the object, achieving two-dimensional size measurement.

4 SIGNAL CONSTRUCTION

In this section, we first establish the mathematical relationship between BFI and CSI. We then reconstruct CSI ratio using BFI.

4.1 The Mathematical Relationship Between CSI and BFI in Diffraction Zone

The data processing from CSI to BFI involves using SVD to decompose CSI, obtaining the matrix V, and then performing a compression decomposition on the V matrix to obtain two types of angles, ϕ and ψ. In light of this, we first study the mathematical relationship between ϕ (ψ) and CSI.

Assume $H_{N \times M}$ is the channel matrix of a subcarrier, where M represents the number of AP's antennas and N represents the number of the node's antennas. The SVD of the channel matrix H is as follows:

$$H = \mathbb{U}\mathbb{S}\mathbb{V}^{\dagger}, \tag{3}$$

where $\mathbb{S}$ is a diagonal matrix with diagonal elements σ_k ($k = 1, \ldots, N_s$) representing the real singular values, and $N_s = \min(N, M)$. $\mathbb{U}$ and $\mathbb{V}$ are the left singular matrix and the right singular matrix, respectively. They are both unitary matrices containing complex elements (with size $N \times N$ and $M \times M$, respectively). $\mathbb{V}^{\dagger}$ denotes the Hermitian transpose of $\mathbb{V}$.

Without loss of generality, assume that there is only one antenna at the node, i.e., $N = 1$. Then, the right singular matrix $\mathbb{V}$ satisfies the following condition:

$$\mathbb{V} = \frac{1}{\sigma}H = \frac{1}{\sqrt{\sum_{p=1}^{M}\left|H(t)_{1,p}\right|^2}}H, \tag{4}$$

where the matrix $\mathbb{V}$ is equal to the CSI amplitude scaled by the singular value σ. The singular value σ is calculated as the square root of the sum of the squares of the CSI amplitudes. As CSI amplitude varies with target movement, σ is time-varying.

Transmitting the entire $\mathbb{V}$ matrix with $N \times M$ complex values incurs significant overhead especially when there are a large number of subcarriers (256). To reduce transmission overhead, the $\mathbb{V}$ matrix is further decomposed and expressed in polar coordinates as two angles ϕ and ψ. The $\mathbb{V}$ matrix can be split into the product of a preprocessing matrix $D_l(\phi)$ and a rotation matrix $G_i^{\dagger}(\psi)$:

$$V = \tilde{D}\left(D_1(\phi)\left[\prod_{l=2}^{M}G_{l1}^{\dagger}(\psi)\right]\right)\mathbb{I}_{M \times 1}, \tag{5}$$

where $\tilde{D}$ is a pre-processing matrix, $D_1(\phi)$ is also a pre-processing matrix which contains the angle ϕ, and $G_{l1}^{\dagger}(\psi)$ is a rotation matrix which contains the angle ψ. $\mathbb{I}_{M \times 1}$ is an $M \times 1$ identity vector, with additional rows filled with zeros. *The beamforming feedback information is a series of angles ϕ and ψ. Compared with the original channel matrix $\mathbb{V}$, BFI does not contain the information of $\tilde{D}$. This omission does not affect communication. However, for sensing, the loss of $\tilde{D}$ means that only the relative information between antennas exits and the absolute amplitude and phase information is missing.*

Based on the derivation, ϕ satisfies the following relationship:

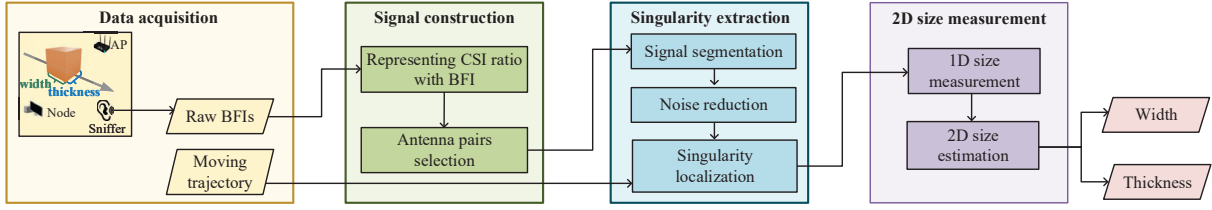$$\phi_{l,1} = \angle(H_{M,1}) - \angle(H_{l,1}) \quad \text{for } l = 2, \ldots, M. \tag{6}$$

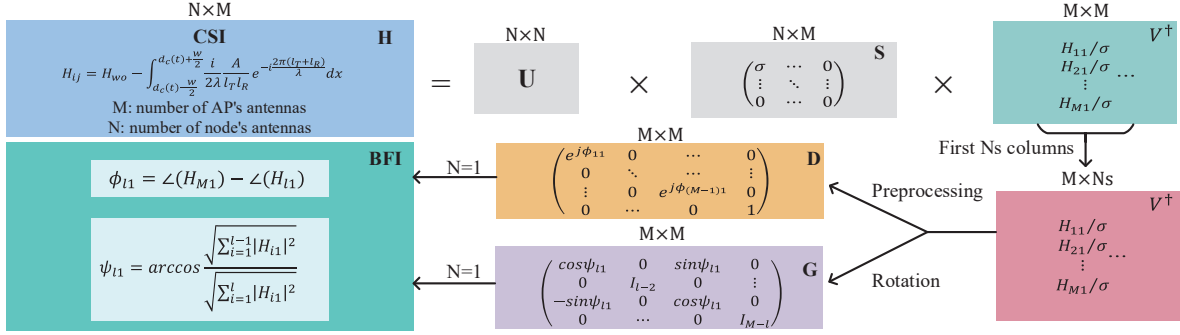**Figure 5: System overview of Wi2DMeasure.**

Figure 6: Conversion from CSI to BFI.

That is, the l-th element of ϕ equals to the phase difference between the l-th antenna and the reference antenna. ψ can be expressed as:

$$
\begin{aligned}
\psi_{l,1} &= \arccos\left(\frac{\sqrt{\sum_{i=1}^{l-1}\left|H_{i,1}\right|^2}}{\sqrt{\sum_{i=1}^{l}\left|H_{i,1}\right|^2}}\right) \\
&= \arcsin\left(\frac{\left|H_{l,1}\right|}{\sqrt{\sum_{i=1}^{l}\left|H_{i,1}\right|^2}}\right) \quad \text{for } l = 2,\dots,M.
\end{aligned}
\tag{7}
$$

ψ describes the difference in signal amplitude space before and after adding the CSI from the l-th antenna. If ψ is close to 0, it means that the new path (i.e., lth path) is almost aligned with the previous paths, contributing little new information for beamforming. If ψ is close to 90 degrees, it means that the new path is orthogonal to the previous paths, adding new information. Figure 6 presents the detailed conversion procedure from CSI to BFI.

4.2 Using BFI for Object Size Measurement

In the previous section, we established the mathematical relationship between BFI and CSI. To achieve two-dimensional size measurement, we represent CSI ratio with BFI and validate its effectiveness for sensing in this section.

4.2.1 Object Measurement with BFI. Based on Section 2.1, the key to measuring object size in the diffraction zone is extracting the singularity information from the signal. We now compare the differences between BFI and CSI on the complex plane through simulation. By letting the same object move 0.15 m away from the LoS, we obtain the CSI and BFI variation patterns as shown in Figure 2. Unlike the CSI trajectory which has singularities, the BFI does not necessarily have singularities, or the positions of singularities vary. Due to the significant differences between BFI and CSI patterns

on the complex plane, existing object size measurement methods based on CSI cannot be directly applied to BFI-based sensing.

4.2.2 Constructing CSI Ratio with BFI. To extract singularity information from BFI, we propose to construct CSI ratio using BFI. Although the amplitude and phase of CSI cannot be directly extracted from BFI, the ϕ of BFI represents the phase difference of CSI between two AP antennas, and the ψ of BFI represents the amplitude ratio of CSI between two AP antennas. This is equivalent to dividing the CSIs of two AP-node links. This indicates that we can construct the CSI ratio using BFI. According to the Möbius theorem [30], the CSI ratio retains the conformality of the CSI, and thus the singularity information is preserved in the CSI ratio. For any two of the AP's antennas p and q, according to Equation 6, the phase of the CSI ratio between them can be expressed as:

$$
\begin{aligned}
\angle\left(\frac{H_{p,1}}{H_{q,1}}\right) &= \angle(H_{p,1}) - \angle(H_{q,1}) \\
&= \angle(H_{p,1}) - \angle(H_{M,1}) + \angle(H_{M,1}) - \angle(H_{q,1}) \\
&= -(\phi_{p,1} - \phi_{q,1}).
\end{aligned}
\tag{8}
$$

Equation 8 indicates that *the difference between the p-th and q-th elements in ϕ equals to the phase difference of the CSIs at the AP's p-th and q-th antenna.* According to Equation 7, the amplitude of the CSI ratio between the p-th and q-th ($p > q$) antenna can be expressed as:

$$
\begin{aligned}
\left|\frac{H_{p,1}}{H_{q,1}}\right| &= \frac{\left|H_{p,1}\right|}{\left|H_{q,1}\right|} \\
&= \frac{\sqrt{\sum_{i=1}^{q}\left|H_{i,1}\right|^2}}{\left|H_{q,1}\right|} \prod_{j=q+1}^{p}\frac{\sqrt{\sum_{i=1}^{j}\left|H_{i,1}\right|^2}}{\sqrt{\sum_{i=1}^{j-1}\left|H_{i,1}\right|^2}} \frac{\left|H_{p,1}\right|}{\sqrt{\sum_{i=1}^{p}\left|H_{i,1}\right|^2}} \\
&= \frac{\sin\psi_{p,1}}{\sin\psi_{q,1}\prod_{i=q+1}^{p}\cos\psi_{i,1}} \quad (p > q).
\end{aligned}
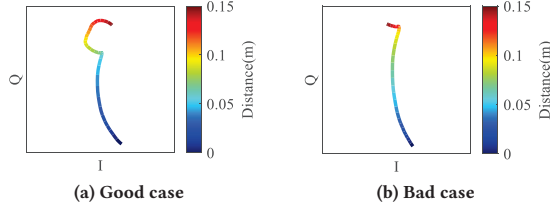\tag{9}
$$

(a) Good case

(b) Bad case

Figure 7: CSI ratio constructed with BFI from different links.

(a) Small antenna spacing

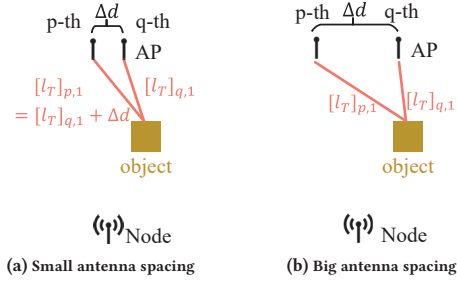**(b) Big antenna spacing**

Figure 8: Impact of antenna spacing on CSI ratio.

Equation 9 shows that *the amplitude ratio of CSI can be represented as a series of trigonometric operations on the p-th and q-th elements of ψ*. Similarly we have:

$$\left| \frac{H_{p,1}}{H_{q,1}} \right| = \frac{\sin \psi_{p,1} \prod_{i=p+1}^{q} \cos \psi_{i,1}}{\sin \psi_{q,1}} \quad (p < q). \tag{10}$$

By combining the phase relationships between CSI ratio and BFI (Equation 8) together with the amplitude relationship between CSI ratio and BFI (Equations 9 and 10), we can fully construct CSI ratio using BFI:

$$\begin{cases} \underbrace{\frac{[H]_{p,1}}{[H]_{q,1}}}_{\text{CSI ratio}} = \underbrace{\frac{\sin \psi_{p,1}}{\sin \psi_{q,1} \prod_{i=q+1}^{p} \cos \psi_{i,1}} e^{-i(\phi_{p1}-\phi_{q1})}}_{\text{BFI Processing}} & (p > q) \\ \frac{[H]_{p,1}}{[H]_{q,1}} = \frac{\sin \psi_{p1} \prod_{i=p+1}^{q} \cos \psi_{i1}}{\sin \psi_{q1}} e^{-i(\phi_{p,1}-\phi_{q,1})} & (p < q) \end{cases}$$
$$\tag{11}$$

This indicates that, although BFI is a compressed version of CSI, we can still construct CSI ratio for sensing as shown in Figure 7a, which contains the same singularity information as that in CSI (Figure 3b).

4.2.3 Selecting Effective Antenna Pair to Construct CSI Ratio Based on Antenna Spacing. From the two CSI ratio patterns constructed with BFI shown in Figure 7, we can see that the constructed CSI ratio patterns with different BFI corresponding to different links are not consistent.

Through further analysis, we find that this is related to the spacing between antennas. Specifically, assuming the distance between the p-th and q-th antennas at the AP is Δd as shown in Figure 8, we can establish a direct mathematical relationship between the

constructed CSI ratio and the signals according to Equation 11 and Equation 1:

$$\frac{\sin \psi_{p1} \prod_{i=p+1}^{q} \cos \psi_{i1}}{\sin \psi_{q1}} e^{-i(\phi_{p,1}-\phi_{q,1})}$$
$$= \frac{[H_{wo}]_{p,1} - \frac{i}{2\lambda} \int_{d_c(t)-\frac{W}{2}}^{d_c(t)+\frac{W}{2}} \frac{A}{[l_T]_{p,1}[l_R]_{p,1}} e^{-i\frac{2\pi \cdot ([l_T]_{p,1}+[l_R]_{p,1})}{\lambda}} dx}{[H_{wo}]_{q,1} - \frac{i}{2\lambda} \int_{d_c(t)-\frac{W}{2}}^{d_c(t)+\frac{W}{2}} \frac{A}{[l_T]_{q,1}[l_R]_{q,1}} e^{-i\frac{2\pi \cdot ([l_T]_{q,1}+[l_R]_{q,1})}{\lambda}} dx}. \tag{12}$$

If Δd is much smaller than the distance from the target to the transceivers (Figure 8a), Equation 12 can be simplified as:

$$\frac{\sin \psi_{p1} \prod_{i=p+1}^{q} \cos \psi_{i1}}{\sin \psi_{q1}} e^{-i(\phi_{p,1}-\phi_{q,1})} \approx \frac{A_p + Z}{A_q + BZ}, \tag{13}$$

where $Z = -\frac{i}{2\lambda} \int_{d_c(t)-\frac{W}{2}}^{d_c(t)+\frac{W}{2}} \frac{A}{[l_T]_{p,1}[l_R]_{p,1}} e^{-i\frac{2\pi \cdot ([l_T]_{p,1}+[l_R]_{p,1})}{\lambda}} dx$ represents the diffraction signal from the object to the node for the p-th AP antenna. We can see that in this case, the constructed CSI ratio satisfies the Möbius transformation, preserving the conformality (e.g., the singularity property) of the original CSIs. Very interestingly, we observe that when the two antennas are separated relatively far away, the constructed CSI ratio does not satisfy the Möbius transformation but still preserves the conformality of one of the CSIs. This is because when two antennas are far away, the target can be close to one of the links and relatively far away from the other link during the process of movement. In this case, the diffraction effect at the close-by link is much stronger than the far-away link and the constructed CSI ratio can be approximated as a CSI because the variation of the far-away link can be ignored and the denominator in Equation 12 can be assumed as a constant. Based on these important findings, we process the BFI-constructed CSI ratio differently accordingly to the spacing between antennas.

5 SINGULARITY POSITION EXTRACTION

In this section, we first introduce how to segment the reconstructed CSI ratio that contains size information. Then, we present our denoising method to extract accurate singularity positions.

5.1 Signal Segmentation

As the constructed CSI ratio involves more than one link, we need to determine which link to use (i.e., at what angle the projection is viewed) when we map the position of singularity point to the target size. When two AP antennas are close to each other, the singularity plots of the two CSIs are similar to each other. In this case, we can use either link. In this work, we propose to use a virtual link in the middle of the two actual links for the best performance as shown in Figure 9a. When the two antennas are far away, the constructed CSI ratio only exhibits the characteristic of the link closer to the target. Thus, we choose the link closer to the target which can be identified with a larger signal variation for size measurement shown in Figure 9b.

We further observe that when the target is closer to the LoS path, the diffraction effect is much stronger, presenting clearer singularity points. Thus, during the process of a target moving across the diffraction zone as shown in Figure 9, we use the signal
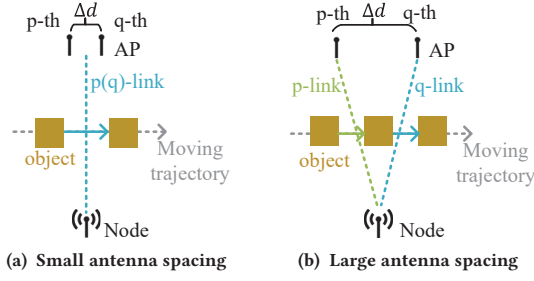
(a) Small antenna spacing   **(b) Large antenna spacing**

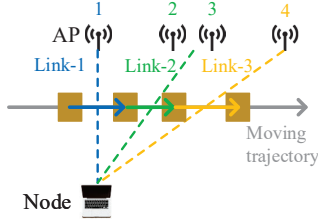**Figure 9: Determining the equivalent link(s) for BFI.**

Figure 10: Signal segmentation for each link.

segment when the target is relatively close to the LoS path of an AP-node antenna pair for size measurement. Based on our experiments, the diffraction effect is strong as long as the boundary of the target is within the range of 25 cm from the LoS path.

We employ an example to illustrate the above concept. As shown in Figure 10, the AP is equipped with four antennas. According to the above analysis, the CSI ratio constructed by the 2nd and 3rd close-by antennas corresponds to link-2, while the CSI ratio constructed by the 1st and 4th farther-away antennas corresponds to link-1 and link-3. When the object moves from left to right, we can extract three signal segments corresponding to three projection views from link-1, link-2 and link-3 respectively.

5.2 Noise Reduction

As shown in Figure 11a, when an object moves across the link, the noise in the BFI and correspondingly constructed CSI ratio extracted from the commodity WiFi device is high. To mitigate the effect of noise $\varepsilon(f_k, t)$, the insight from Wiener-chinchin law of large numbers suggests that statistically averaging a large number of observations of the same noisy signal can effectively reduce the noise level [4]. This approach is based on the fact that the sample mean of a large number of independent observations will converge to the true mean, thereby diluting the random noise present in individual observations. To save the power consumption, storage and transfer load, the sample rate of BFI on commodity devices is usually quite low. To increase the number of observations, we upsample the data and utilize readings from multiple subcarriers.

Even when the signal is affected by human activities, it still exhibits stability within a short period (e.g., 0.02 s). This temporal stability presents us the opportunity to upsample the data. We employ linear interpolation to better preserve the local characteristics of the signal, especially near singularity points, avoiding the smoothing effect caused by other interpolation schemes such as
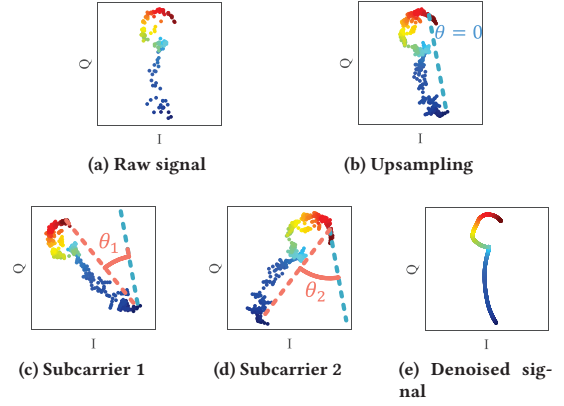

(a) Raw signal   **(b) Upsampling**

(c) Subcarrier 1   **(d) Subcarrier 2**   **(e) Denoised signal**

Figure 11: Upsample the data and utilize readings from multiple subcarriers for noise reduction.

(a) Curvature calculation   **(b) Curvature variations**
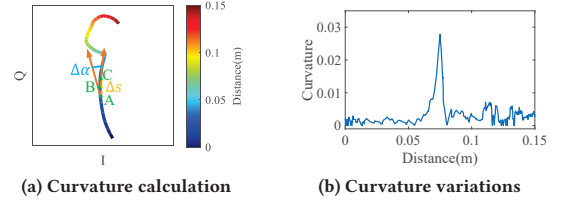
Figure 12: Extracting singularities with curvature feature.

mean interpolation. Figure 11b shows the results of upsampling the signal and a larger number of data points are generated.

By leveraging the larger number of subcarriers available at commodity WiFi hardware (e.g., 256 for 802.11 ac), we can collect more data samples, each representing an independent observation of the signal. However, the signal trajectories captured from different subcarriers exhibit a different angle rotation as shown in Figure 11c and Figure 11d. We thus search the phase adjustment to make the subcarriers aligned at the same angle and average them as below:

$$
\begin{aligned}
C(t) &= \frac{1}{K} \sum_{i=1}^{K} \left(\frac{[H(f_i, t)]_{p,1}}{[H(f_i, t)]_{q,1}} + \varepsilon(f_i, t) \right) e^{j\theta_i} \\
&= \frac{1}{K} \sum_{i=1}^{K} \frac{[H(f_i, t)]_{p,1}}{[H(f_i, t)]_{q,1}} e^{j\theta_i} + \frac{1}{K} \sum_{i=1}^{K} \varepsilon(f_i, t) e^{j\theta_i}
\end{aligned}
\tag{14}
$$

where θ_i represents the phase adjustment of the signals on each subcarrier. The noise part $\varepsilon(f_i, t) e^{j\theta_i}$ follows a normal distribution with zero mean and with a large number of samples, $\frac{1}{K} \sum_{i=1}^{K} \varepsilon(f_i, t) e^{j\theta_i}$ approaches 0 [27]. This method reduces environmental noise and improves the signal-to-noise ratio without distorting the singularity information as shown in Figure 11e.

5.3 Singularity Position Extraction

To detect singularities, we identify points where the signal vector direction changes sharply over time. Mathematically, we use curvature to describe the rate of direction change. If we know three adjacent points on a CSI trajectory (e.g., A, B, and C, as shown in Figure 12a), we can calculate the curvature of these three points. Specifically, $\overrightarrow{AB}$ and $\overrightarrow{BC}$ represent the adjacent tangent vectors, and Δs represents the arc length between A and C. When the arc length
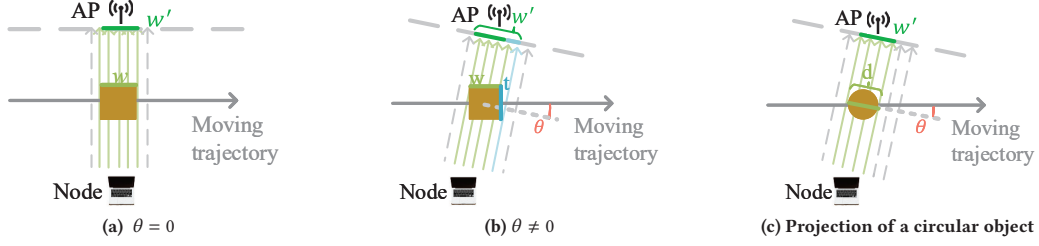
Figure 13: Relationship between the measured projection length and actual size at different angles.

Δs approaches 0, the curvature κ at point B is calculated as:

$$\kappa = \lim_{\Delta s \to 0} \left| \frac{\alpha(\overrightarrow{AB}) - \alpha(\overrightarrow{BC})}{\Delta s} \right| = \lim_{\Delta s \to 0} \left| \frac{\Delta \alpha}{\Delta s} \right|, \qquad (15)$$

where $\Delta \alpha$ represents the change of direction between adjacent tangent vectors. As shown in Figure 12b, we present the curvature graph of an object moving along the perpendicular bisector of the AP's and node's antennas. Due to the very high curvature values at singularity points, a simple peak detection algorithm can achieve robust singularity detection. Combined with the object's motion trajectory information, we can calculate the positions where singularities appear.

6 2D SIZE MEASUREMENT USING MULTIPLE ANTENNA PAIRS

We now introduce how to employ CSI ratios from multiple antenna pairs to calculate the size, i.e., width and thickness of the object.

6.1 1D Size Measurement

To calculate the one-dimensional size of an object, we start by considering the position of the singularity. As detailed in Section 2.1, singularities on the signal curve arise when the path length difference at the object's edges equals to an integer multiple of the wavelength. This phenomenon allows us to establish a relationship between the object's one-dimensional projection size w' and the singularity position P_s. From the trajectory in Figure 12, we can tell the actual physical location where the singularity occurs. Specifically, the color indicates the distance (d_s) between the physical location of the singularity point and the LoS path. The quantitative relationship between d_s and the projection size w' can thus be expressed as the following equation:

$$\left(\sqrt{l_{To} + \left(d_s + \frac{w'}{2}\right)^2} + \sqrt{l_{Ro} + \left(d_s + \frac{w'}{2}\right)^2} \right) -$$
$$\left(\sqrt{l_{To} + \left(d_s - \frac{w'}{2}\right)^2} + \sqrt{l_{Ro} + \left(d_s - \frac{w'}{2}\right)^2} \right) = k\lambda. \qquad (16)$$

Given the positions of the WiFi devices (i.e., AP and node) and the object's movement trajectory, l_{To} and l_{Ro} can be calculated from the physical position of the singularity points and the locations of the AP and node. Thus, in the above equation, the only unknown variable is the one-dimensional projection size of the object, w'. By solving this equation for each link formed by one antenna pair, we can determine the one-dimensional projection size w' using the measured singularity distance d_s. The one-dimensional projection size refers to the length of the object's size projection at the direction perpendicular to the antenna pair link.

To mathematically express the relationship between the projection size and the object's true size, we define the angle θ between the projection direction and the object's motion direction (x-axis) in Figure 13b. When θ is 0 degrees, the projection length w' measured equals to the object's width w. When θ is not 0 degrees, the measured projection length w' is a combination of the object's width w and thickness t which can be described by the following equation:

$$w' = w \cdot \cos \theta + t \cdot \sin \theta. \qquad (17)$$

If the object is not rectangular but other shapes, the relationship between the projection length and the actual size changes accordingly. For example, for a circular object shown in Figure 13c, the projection length w' is only related to the diameter d of the object and is independent of the angle θ, which can be expressed as $w' = d$. The proposed system can be applied to measure object size of different shapes.

6.2 2D Size Measurement

As illustrated in Section 6.1, the projection size is dependent on the angle between projection direction and target moving direction. The relationship between the projection length $w'(\theta)$ and the object's actual width w and thickness t is described as Equation 17. With multiple links, we can obtain multiple equations. We apply the least squares method to find the optimal values of w and t that best satisfy all the equations. Specifically, we achieve this by minimizing the following objective function:

$$J(w, t) = \sum_{i=1}^{n} \left(w'(\theta_i) - (w \cdot \cos \theta_i + t \cdot \sin \theta_i) \right)^2, \qquad (18)$$

where n is the number of equations, and $w'(\theta_i)$ is the projection length at the i-th angle θ_i. To solve the above minimization problem, we adopt linear regression which is commonly used for minimizing the objective function to estimate the values of w and t. We rewrite Equation 18 in matrix form:

$$\mathbf{A}\mathbf{x} = \mathbf{b}, \qquad (19)$$

where

$$\mathbf{A} = \begin{bmatrix} \cos \theta_1 & \sin \theta_1 \\ \cos \theta_2 & \sin \theta_2 \\ \vdots & \vdots \\ \cos \theta_n & \sin \theta_n \end{bmatrix}, \quad \mathbf{x} = \begin{bmatrix} w \\ t \end{bmatrix}, \quad \mathbf{b} = \begin{bmatrix} w'(\theta_1) \\ w'(\theta_2) \\ \vdots \\ w'(\theta_n) \end{bmatrix},$$
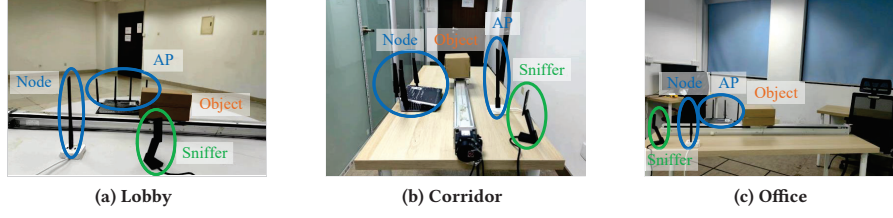
(a) Lobby

(b) Corridor

(c) Office

Figure 14: Typical indoor environments.
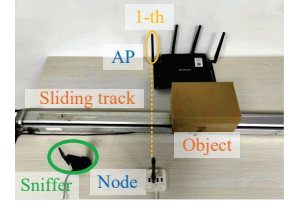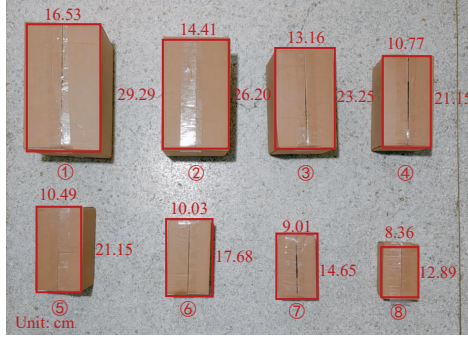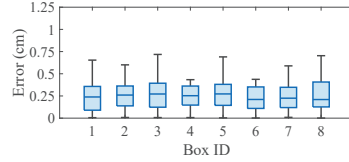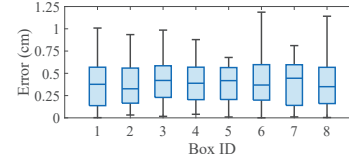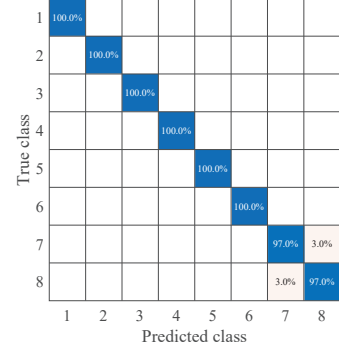

Figure 15: System setup.

Figure 16: Box sizes

(a) Width measurement error

(b) Thickness measurement error

(c) Confusion matrix

Figure 17: Overall performance.

By solving the matrix equation $\mathbf{A}^{\top}\mathbf{A}\mathbf{x} = \mathbf{A}^{\top}\mathbf{b}$, we can obtain the optimal solution $\mathbf{x} = \begin{bmatrix} w & t \end{bmatrix}^{\top}$, which are the width and thickness of the target.

7 EVALUATION

7.1 Experiment Setup

Implementation: We use a Netgear R7800 router equipped with Qualcomm WiFi QCA9984 chipset as the AP and a Tenda U10 card as the WiFi node. Our system operates at a central frequency of 5.32 GHz, and the channel bandwidth is 80 MHz. We use a Netgear A6210 as a sniffer to capture BFI packets. We use the iperf3 tool [18] to generate UDP traffic from the AP to the node that triggers MU-MIMO transmissions.

Experiment setup: We conduct experiments in three typical indoor environments: a large hall with little multipath (10 m × 8 m), a corridor with certain multipath (6 m × 2 m), and an office with rich multipath (4 m × 3 m), as shown in Figure 14. In each environment, we deploy Wi2DMeasure as shown in Figure 15. During the experiment, we move the target along the sliding track at a speed of 0.12 m/s. The default moving distance is 1.2 m. The default distance between the WiFi AP and the node is 0.5 m.

Ground truth measurement: The ground truth is measured using a vernier caliper with an accuracy of 0.05 mm [20]. The difference between the measured size and the ground truth size is the size measurement error.

7.2 Overall Performance

To evaluate the overall performance of Wi2DMeasure, we first use standard shipping boxes of varying widths and thicknesses

which are commonly used in logistics as targets. For each target, we repeat the experiment five times to ensure consistency and reliability of the results. Figure 16 shows the width and thickness of eight different-sized boxes tested in our experiment. Figure 17a and Figure 17b show the absolute estimation errors for the object's width and thickness measurements, respectively. In all the cases, the median error is smaller than 0.6 cm which is a surprisingly accurate result for WiFi-based size measurement. We also notice that the width error is slightly smaller than the thickness error. We believe this is because under the current device placement, the projection length contains more width information.

Note that in real-life logistics, the boxes need to be grouped based on size. We thus use the obtained size measurements to group the boxes. Specifically, we compared the obtained sizes with the eight ground truths and put the box in the group with the smallest difference. Figure 17c shows the classification accuracy. We can see that the classification accuracy for boxes 1 to 6 is always 100%. A slightly lower accuracy (i.e., 97%) is achieved with boxes 7 and 8 because they are small and their thickness differ by only 0.6 cm.

7.3 Comparison with SOTA Work

We further compare the proposed system with the state-of-the-art work WiMeasure [43], a 1D size measurement system based on CSI. For a fair comparison, we downgrade our system to perform 1D size measurement. In this experiment, we use only a single pair of transceivers, following the same setup as described in Section 7.1. The results are shown in Figure 18. The measurement errors of the proposed system are consistently lower than those achieved with WiMeasure. This is because WiMeasure relies on the number of
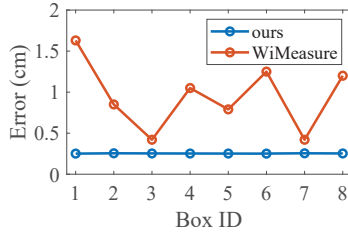
Figure 18: Comparason with WiMeasure.

(a) RT-AC86U

(b) R7800

(c) WDR7660

(d) WDR7661

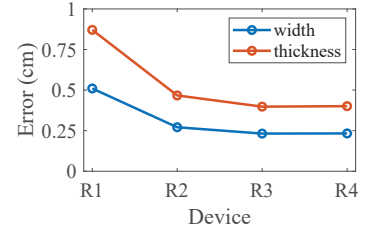Figure 19: All tested routers support MU-MIMO technology.

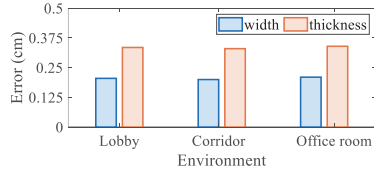Figure 20: Impact of device type.
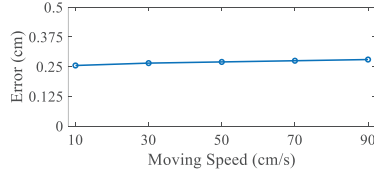
Figure 21: Impact of moving speed.

Figure 22: Impact of environment.

(a) Metal box.

(b) Wood box.
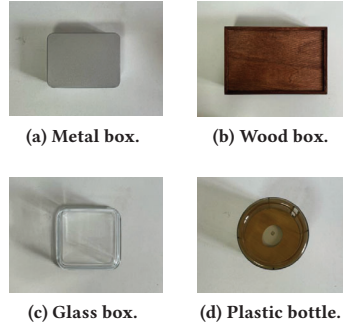
(c) Glass box.

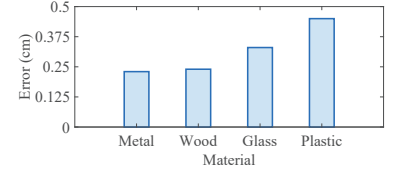(d) Plastic bottle.

Figure 23: Different kinds of material.

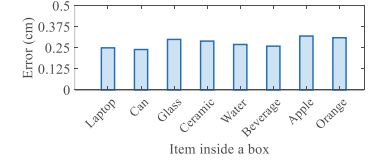Figure 24: Impact of target material.

Figure 25: Impact of items inside a box.

singularities for estimation whereas our system utilizes the more fine-grained singularity position information for size estimation.

7.4 System Robustness

Next, we investigate possible factors that may affect the sensing performance, including device type, object moving speed, environment, target material, item inside the box, antenna height, and surrounding interference.

7.4.1 Impact of Device Type. To demonstrate the generality of our method, we test our system with four different WiFi routers, including the Asus RT-AC86U, Netgear R7800, TP-LINK WDR7660, and TP-LINK WDR7661, equipped with 3, 4, 6, and 6 antennas, respectively, as shown in Figure 19. These routers are denoted as R1 to R4. Although these routers are of different brands and embedded with different WiFi chips, we are able to successfully collect BFI from all of them without modifying any firmware or drivers. Figure 20 shows that Wi2DMeasure can achieve accurate two-dimensional size measurements with all these routers. We also observe that more antennas can bring higher accuracy because a larger number of antennas can provide more measurements from different angles.

7.4.2 Impact of Moving Speed. The speed of the conveyor belt ranges from 10 cm/s to 70 cm/s. Industrial assembly lines typically move at speeds of 10-20 cm/s. Figure 21 shows that Wi2DMeasure can achieve accurate two-dimensional size measurements under a wide range of motion speeds. For instance, increasing the object

speed from 10 cm/s to 90 cm/s only slightly increases the measurement error by about 0.1 cm. Note that a higher sampling rate can be used to measure the size of a target moving at higher speeds.

7.4.3 Impact of Different Environments. In this set of experiments, we evaluate Wi2DMeasure in three different indoor environments as shown in Figure 14. Figure 22 shows the absolute measurement errors. It can be seen that Wi2DMeasure performs robustly in all environments. The impact of multipath on performance is minimal because we use curvature to detect singularity points, and curvature information is independent of signals reflected from static objects such as walls and furniture.

7.4.4 Impact of Target Material. To evaluate the impact of material, we test a metal box, a wood box, a glass box, and a plastic bottle, as shown in Figure 23. Figure 24 shows the average measurement error for metal objects (0.22 cm) is the smallest. The average errors for wood and glass are 0.25 cm and 0.26 cm, respectively. The plastic has the largest average error (0.41 cm). We believe this is because metal has the strongest diffraction effect, while plastic can absorb a large amount of signal power.

7.4.5 Impact of Items Inside the Box. We further verify the impact of different items inside the box on the measurement performance. We place items made of metal (i.e., laptop and can), non-metallic objects (i.e., glass photo frame and ceramic jar), liquids (i.e., mineral water and beverage), and fruits (i.e., apple and orange) inside the box. Figure 25 shows the errors of Wi2DMeasure when measuring boxes containing different items. We observe that with different
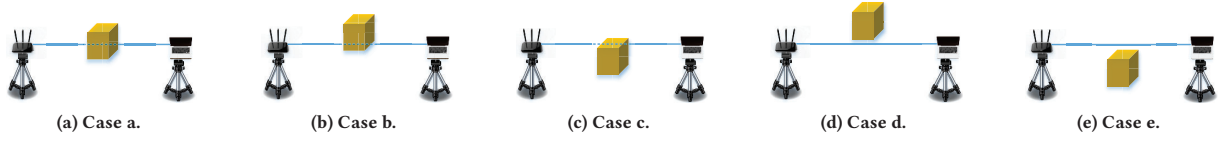
(a) Case a.   (b) Case b.   (c) Case c.   (d) Case d.   (e) Case e.

Figure 26: Target size measurement at different antenna heights.
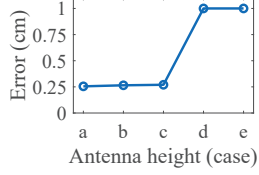
Figure 27: Impact of antenna height.

Figure 28: Impact of interference.

(a) Apple grading based on size

(b) Asymmetrical apples

(c) Symmetrical apple

Figure 29: Grading apples by size and symmetry.
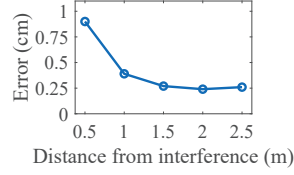
items inside the box, the width and thickness measurement errors remain within 0.375 cm. This is because our system relies on diffraction signals that go around the surface of the box and thus are independent of the items inside the box.

7.4.6 Impact of Antenna Height. To evaluate the impact of antenna height, we fix the position of the sliding track where the object is located and adjust the antenna height to five positions as shown in Figure 26: (a) the object's center blocks the LoS path of the antenna pair (Figure 26a), (b) the object's lower edge just touches the LoS path of the antenna pair (Figure 26b), (c) the object's upper edge just touches the LoS path (Figure 26c), (d) the object is above and (e) below the LoS path (Figures 26d and 26e). Figure 27 shows that the experiment results match the theoretical results well, indicating that a small antenna height change has little impact on the performance. The performance only decays when the antenna height is too low or too high. Therefore, when the system is deployed in practice, the user is suggested to adjust the antenna height to ensure that the LoS path is roughly at the same height of the target.

7.4.7 Impact of Interference from Surrounding People. To evaluate the impact of interference from surrounding people, we instruct an interferer to move along the perpendicular bisector of the LoS path. We vary the distance between the interferer and the target from 0.5 m to 2.5 m at a step size of 0.5 m. From Figure 28, we observe that when the interferer is more than 1 m away from the target, the achieved error is close to that without an interferer. This indicates that when the interferer is more than 1 m away, the induced interference has a negligible effect on the sensing performance. When the interferer is 0.5 m away from the target, the error is 0.98 cm, which is still good enough for most applications. This is because compared to the reflections from further away interferers, the diffraction signals in the first Fresnel zone near the LoS path utilized by our system for sensing is stronger.

7.5 Performance of Other Applications

7.5.1 Grading Apples by Size and Symmetry. To demonstrate the practical application of our WiFi measurement system, we evaluate its performance in measuring the fruit size. Accurate measurement
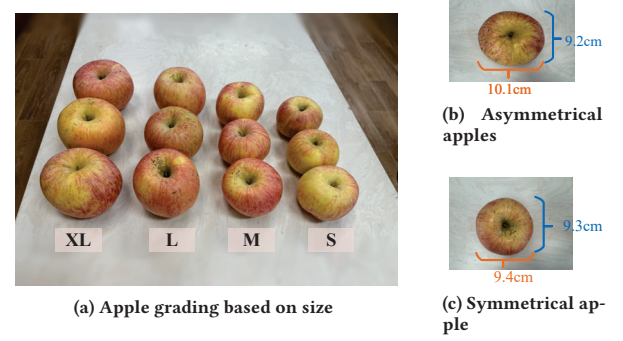
of fruit size is crucial for quality control and pricing. By analyzing the diffraction signal caused by the fruit, we can measure its diameter, realizing a non-invasive solution for fruit grading.

During the measurement process, we randomly select 15 apples with diameters ranging from 6.2 cm to 9.8 cm. Wi2DMeasure measures the diameter of each apple using the method in Section 6. Following the apple grading standard [33], we classify the apples into extra-large (diameter greater than 8.9 cm), large (diameter between 7.9 cm and 8.9 cm), medium (diameter between 6.6 cm and 7.9 cm), and small (diameter smaller than 6.6 cm). The true sizes of the apples are measured using a vernier caliper with an accuracy of 0.01 mm. Figure 29a shows the size-based apple grouping based on our method and 100% classification accuracy can be achieved.

For apple grading, it is also necessary to evaluate their symmetry level in addition to the size. As shown in Figure 29b, the diameters of an apple vary across dimensions. Wi2DMeasure can obtain the projection length of an apple from different directions, telling whether the apple is symmetrical for more advanced grading.

7.5.2 Measuring the Size of an Object Inside a Paper or Plastic Bag. Since WiFi signals can penetrate opaque materials, we measure the size of a metal tin inside a paper bag and an aluminum can inside a plastic pad in this experiment. Note that to sense the target inside a box, the WiFi signals need to penetrate through the box twice, therefore, the diffracted signals from the target become extremely weak. Because of this, the proposed system can only sense a target inside a thin box such as a plastic bag or a paper bag. For a target inside a thicker box such as the cardboard box in Section 7.2, our system is not able to sense the target inside but captures the size of the cardboard box. As shown in Figure 30b, the actual width and thickness of the metal tin are 15.88 cm and 10.22 cm, respectively. Wi2DMeasure measures the width and thickness of the tin as 15.53 cm and 9.97 cm. The measurement errors for both width and thickness are less than 0.4 cm. Figure 30d shows that the actual diameter of the aluminum can is 8.01 cm, and Wi2DMeasure

| (a) Outside | (b) Inside | (c) Outside | (d) Inside |

Figure 30: Measuring the size of object inside.

measures the diameter as 8.23 cm, with a small error of 0.22 cm. It is thus possible for the proposed system to measure the size of objects without opening the package.

8 RELATED WORK

In this section, we introduce RF-based object size measurement and existing sensing work using BFI/BFM.

8.1 RF-based Object Size Image or Measurement

Research on RF-based imaging began in the late 1970s [9]. Various technologies including millimeter-wave radar [13, 40, 46, 53], terahertz radar [5–7, 11], and LiDAR [16, 21, 28, 55, 58], have been explored for imaging and size measurement. These technologies primarily rely on reconstructing the target's point cloud by precisely measuring the parameters of reflected signals, such as Time of Flight (ToF), Angle of Arrival (AoA), and Doppler Frequency Shift (DFS). High frequencies and large antenna arrays are required to form narrow signal beam, and a wide bandwidth is needed to obtain accurate time information. For instance, RF-Capture [2] employs a bandwidth of 1.78 GHz and a 4×16 antenna array to capture the skeletal information of a human target. Similarly, MilliPoint [36] leverages commercial millimeter-wave radar with a bandwidth of 4 GHz and a 6×8 antenna array to achieve a median height estimation error less than 5 cm.

Low-frequency signals such as WiFi (e.g., 2.4 GHz or 5 GHz) still face challenges for imaging or size measurement due to their narrow bandwidth. WiFi-based target imaging methods utilize both reflection signals [17, 19, 22, 37] and diffraction signals [34, 43, 51] for size measurement. To address the issue of limited number of antennas, recent studies propose to create a virtual antenna array by moving the transceiver's antennas [17, 37]. While effective in locating targets, these methods can only capture very coarse shape information. Diffraction-based techniques like Wiffract [34] use Keller cone diffraction to fit object edges. The accuracy is still low and it can only classify objects without the capability of measuring the size. WiMeasure [43] measures object size using the number of signal singularities but requires multiple transceiver pairs and can only achieve one-dimensional measurement. WiProfile [51] measures object width and height contours via the Fresnel inverse transform. It requires complete CSI information and is not suitable for measurements with BFI signals.

Note that although LiDAR and radar can capture the shape information of a target, obtaining accurate size information is still challenging. Typically, distance and signal strength data are required to infer the target size. However, even with advanced signal

processing and machine learning techniques, the accuracy of size measurement is still limited to a few centimeters [8]. Besides, Unlike camera-based methods, Wi2DMeasure is less affected by environmental factors such as lighting conditions.

8.2 BFI and BFM Sensing

In the field of wireless sensing based on WiFi signals, research on BFI and Beamforming Feedback Matrix (BFM) has just started [14, 41, 48, 52]. BeamSense [14] employs a VGG-based Convolutional Neural Network (CNN) to obtain the correlation between BFI data and human activities, successfully classifying 20 different human activities. BFMSense [52] establishes the mathematical relationship between CSI changes and target activities in the reflection zone, which can effectively sense target breathing and moving trajectories. MuKI-Fi [41] adopts adversarial learning techniques to study the relationship between user keystroke activities and signal variations in the diffraction zone.

While these studies demonstrate the potential of using BFI and BFM for motion tracking, we move one step further to use BFI for size measurement. Our work quantitatively analyzes the mathematical relationship between BFI and CSI and achieves a sensing accuracy comparable to CSI. Moving from CSI to BFI presents a new alternative for WiFi sensing.

9 DISCUSSION

Measuring the size of a static object: Compared with traditional reflection-based methods which can image static objects, it is still difficult for the proposed system to measure the size of a static object. However, conventional reflection-based methods require a large bandwidth to achieve a fine-grained resolution to obtain accurate point cloud. We believe the proposed system can complement existing systems in many real-world scenarios.

Objects with irregular shapes: If the target has an irregular shape, or is placed on the belt with an unknown orientation, it is challenging for our system to accurately measure its size. This limitation is mainly due to the limited number of antennas (2-6) at the commodity WiFi APs. By increasing the number of antennas, it is possible for the proposed system to mitigate these issues with projection views from more antenna pairs. For new-generation WiFi protocols, it is fair to assume a setup with one AP and multiple nodes which can provide us with more projection views.

Impact of humidity and temperature variations: For our current deployment with a relatively short propagation distance, humidity and temperature have minimal impact on the propagation of electromagnetic waves with a frequency below 10 GHz [59].

10 CONCLUSION

In this work, for the first time, we make WiFi-based two-dimensional target size measurement possible by analyzing the positions of singularities as the target moves through the diffraction region. Comprehensive experiments demonstrate the effectiveness of the proposed system in estimating the two-dimensional sizes of everyday objects of varying sizes and materials.

REFERENCES

[1] Heba Abdelnasser, Moustafa Youssef, and Khaled A. Harras. 2015. WiGest: A ubiquitous WiFi-based gesture recognition system. In *2015 IEEE Conference on Computer Communications (INFOCOM)*. 1472–1480. https://doi.org/10.1109/INFOCOM.2015.7218525

[2] Fadel Adib, Chen-Yu Hsu, Hongzi Mao, Dina Katabi, and Frédo Durand. 2015. Capturing the human figure through a wall. 34, 6, Article 219 (nov 2015), 13 pages. https://doi.org/10.1145/2816795.2818072

[3] Amazon. 2024. Top 10 Best Selling Access Points. https://www.amazon.com/Best-Sellers-Computer-Networking-Wireless-Access-Points/zgbs/pc/1194486. Data extracted from the list of best sellers on Amazon. Accessed on June 29, 2024.

[4] Julius S Bendat and Allan G Piersol. 2011. *Random data: analysis and measurement procedures*. John Wiley & Sons.

[5] K. B. Cooper, R. J. Dengler, G. Chattopadhyay, E. Schlecht, J. Gill, A. Skalare, I. Mehdi, and P. H. Siegel. 2008. A High-Resolution Imaging Radar at 580 GHz. *IEEE Microwave and Wireless Components Letters* 18, 1 (2008), 64–66. https://doi.org/10.1109/LMWC.2007.912049

[6] Ken B. Cooper, Robert J. Dengler, Nuria Llombart, Tomas Bryllert, Goutam Chattopadhyay, Erich Schlecht, John Gill, Choonsup Lee, Anders Skalare, Imran Mehdi, and Peter H. Siegel. 2008. Penetrating 3-D Imaging at 4- and 25-m Range Using a Submillimeter-Wave Radar. *IEEE Transactions on Microwave Theory and Techniques* 56, 12 (2008), 2771–2778. https://doi.org/10.1109/TMTT.2008.2007081

[7] Ken B. Cooper, Robert J. Dengler, Nuria Llombart, Bertrand Thomas, Goutam Chattopadhyay, and Peter H. Siegel. 2011. THz Imaging Radar for Standoff Personnel Screening. *IEEE Transactions on Terahertz Science and Technology* 1, 1 (2011), 169–182. https://doi.org/10.1109/TTHZ.2011.2159556

[8] Irfan C Engin, Norbert H Maerz, Kenneth J Boyko, and Robert Reals. 2020. Practical measurement of size distribution of blasted rocks using LiDAR scan data. *Rock Mechanics and Rock Engineering* 53 (2020), 4653–4671.

[9] B.R. Feingold and B.J. Levin. 1970. Millimeter Wave Imaging. In *G-MTT 1970 International Microwave Symposium*. 126–130. https://doi.org/10.1109/GMTT.1970.1122786

[10] Chao Feng, Jie Xiong, Liqiong Chang, Ju Wang, Xiaojiang Chen, Dingyi Fang, and Zhanyong Tang. 2019. WiMi: Target Material Identification with Commodity Wi-Fi Devices. In *2019 IEEE 39th International Conference on Distributed Computing Systems (ICDCS)*. 700–710. https://doi.org/10.1109/ICDCS.2019.00075

[11] Fabian Friederich, Wolff von Spiegel, Maris Bauer, Fanzhen Meng, Mark D. Thomson, Sebastian Boppel, Alvydas Lisauskas, Bernd Hils, Viktor Krozer, Andreas Keil, Torsten Löffler, Ralf Henneberger, Anna Katharina Huhn, Gunnar Spickermann, Peter Haring Bolivar, and Hartmut G. Roskos. 2011. THz Active Imaging Systems With Real-Time Capabilities. *IEEE Transactions on Terahertz Science and Technology* 1, 1 (2011), 183–200. https://doi.org/10.1109/TTHZ.2011.2159559

[12] Ruiyang Gao, Mi Zhang, Jie Zhang, Yang Li, Enze Yi, Dan Wu, Leye Wang, and Daqing Zhang. 2021. Towards Position-Independent Sensing for Gesture Recognition with Wi-Fi. *Proceedings of the ACM on Interactive, Mobile, Wearable and Ubiquitous Technologies* 5, 2 (2021), 1–28.

[13] Junfeng Guan, Sohrab Madani, Suraj Jog, Saurabh Gupta, and Haitham Hassanieh. 2020. Through Fog High-Resolution Imaging Using Millimeter Wave Radar. In *2020 IEEECVF Conference on Computer Vision and Pattern Recognition (CVPR)*. 11461–11470. https://doi.org/10.1109/CVPR42600.2020.01148

[14] Khandaker Foysal Haque, Milin Zhang, Francesca Meneghello, and Francesco Restuccia. 2023. BeamSense: Rethinking Wireless Sensing with MU-MIMO Wi-Fi Beamforming Feedback. *arXiv preprint arXiv:2303.09687* (2023).

[15] Wenfeng He, Kaishun Wu, Yongpan Zou, and Zhong Ming. 2015. WiG: WiFi-Based Gesture Recognition System. In *2015 24th International Conference on Computer Communication and Networks (ICCCN)*. 1–7. https://doi.org/10.1109/ICCCN.2015.7288485

[16] Wolfgang Hess, Damon Kohler, Holger Rapp, and Daniel Andor. 2016. Real-time loop closure in 2D LIDAR SLAM. In *2016 IEEE International Conference on Robotics and Automation (ICRA)*. 1271–1278. https://doi.org/10.1109/ICRA.2016.7487258

[17] Donny Huang, Rajalakshmi Nandakumar, and Shyamnath Gollakota. 2014. Feasibility and limits of wi-fi imaging. In *Proceedings of the 12th ACM Conference on Embedded Network Sensor Systems* (Memphis, Tennessee) *(SenSys '14)*. Association for Computing Machinery, New York, NY, USA, 266–279. https://doi.org/10.1145/2668332.2668344

[18] Iperf.fr. [n. d.]. iPerf - The ultimate speed test tool for TCP, UDP and SCTP. https://iperf.fr/. Accessed: 2024-06-19.

[19] Wenjun Jiang, Hongfei Xue, Chenglin Miao, Shiyang Wang, Sen Lin, Chong Tian, Srinivasan Murali, Haochen Hu, Zhi Sun, and Lu Su. 2020. Towards 3D human pose construction using wifi. In *Proceedings of the 26th Annual International Conference on Mobile Computing and Networking* (London, United Kingdom) *(MobiCom '20)*. Association for Computing Machinery, New York, NY, USA, Article 23, 14 pages. https://doi.org/10.1145/3372224.3380900

[20] Kynup. 2024. Measuring Tool Review. https://kynup.shop/measuring-tool/e4CfeB634.html. Accessed: 2024-07-01.

[21] Alex H. Lang, Sourabh Vora, Holger Caesar, Lubing Zhou, Jiong Yang, and Oscar Beijbom. 2019. PointPillars: Fast Encoders for Object Detection From Point

[22] Chenning Li, Zheng Liu, Yuguang Yao, Zhichao Cao, Mi Zhang, and Yunhao Liu. 2020. Wi-fi see it all: generative adversarial network-augmented versatile wi-fi imaging. In *Proceedings of the 18th Conference on Embedded Networked Sensor Systems* (Virtual Event, Japan) *(SenSys '20)*. Association for Computing Machinery, New York, NY, USA, 436–448. https://doi.org/10.1145/3384419.3430725

[23] Shengjie Li, Xiang Li, Kai Niu, Hao Wang, Yue Zhang, and Daqing Zhang. 2017. AR-Alarm: An Adaptive and Robust Intrusion Detection System Leveraging CSI from Commodity Wi-Fi. In *Enhanced Quality of Life and Smart Living*, Mounir Mokhtari, Bessam Abdulrazak, and Hamdi Aloulou (Eds.). Springer International Publishing, Cham, 211–223.

[24] Shengjie Li, Zhaopeng Liu, Yue Zhang, Qin Lv, Xiaopeng Niu, Leye Wang, and Daqing Zhang. 2020. WiBorder: Precise Wi-Fi based Boundary Sensing via Through-wall Discrimination. 4, 3, Article 89 (sep 2020), 30 pages. https://doi.org/10.1145/3411834

[25] Xiang Li, Shengjie Li, Daqing Zhang, Jie Xiong, Yasha Wang, and Hong Mei. 2016. Dynamic-MUSIC: Accurate Device-Free Indoor Localization *(UbiComp '16)*. Association for Computing Machinery, New York, NY, USA, 196–207. https://doi.org/10.1145/2971648.2971665

[26] Xiang Li, Daqing Zhang, Qin Lv, Jie Xiong, Shengjie Li, Yue Zhang, and Hong Mei. 2017. IndoTrack: Device-Free Indoor Human Tracking with Commodity Wi-Fi. 1, 3, Article 72 (Sept. 2017), 22 pages. https://doi.org/10.1145/3130940

[27] Yang Li, Dan Wu, Jie Zhang, Xuhai Xu, Yaxiong Xie, Tao Gu, and Daqing Zhang. 2022. DiverSense: Maximizing Wi-Fi Sensing Range Leveraging Signal Diversity. *Proc. ACM Interact. Mob. Wearable Ubiquitous Technol.* 6, 2, Article 94 (jul 2022), 28 pages. https://doi.org/10.1145/3536393

[28] Yanchao Li, Yanling Yang, Xuesong Xia, Long Gao, Haifang Cong, and Chunhui Wang. 2009. The method for dual-beam laser heterodyne ultra-precision measurement of the glass thickness. In *2009 Conference on Lasers & Electro Optics & The Pacific Rim Conference on Lasers and Electro-Optics*. 1–2. https://doi.org/10.1109/CLEOPR.2009.5292079

[29] Xuefeng Liu, Jiannong Cao, Shaojie Tang, and Jiaqi Wen. 2014. Wi-Sleep: Contactless Sleep Monitoring via WiFi Signals. In *2014 IEEE Real-Time Systems Symposium*. 346–355. https://doi.org/10.1109/RTSS.2014.30

[30] Tristan Needham. 2023. *Visual complex analysis*. Oxford University Press.

[31] Kai Niu, Xuanzhi Wang, Fusang Zhang, Rong Zheng, Zhiyun Yao, and Daqing Zhang. 2022. Rethinking Doppler Effect for Accurate Velocity Estimation With Commodity WiFi Devices. *IEEE Journal on Selected Areas in Communications* 40, 7 (2022), 2164–2178. https://doi.org/10.1109/JSAC.2022.3155523

[32] Kai Niu, Fusang Zhang, Jie Xiong, Xiang Li, Enze Yi, and Daqing Zhang. 2018. Boosting Fine-Grained Activity Sensing by Embracing Wireless Multipath Effects. In *Proceedings of the 14th International Conference on Emerging Networking EXperiments and Technologies* (Heraklion, Greece) *(CoNEXT '18)*. Association for Computing Machinery, New York, NY, USA, 139–151. https://doi.org/10.1145/3281411.3281425

[33] United States Department of Agriculture. 2024. Marketing and Agricultural Product Standard Guidelines. http://www.ams.usda.gov/standards Accessed on: Full access date.

[34] Anurag Pallaprolu, Belal Korany, and Yasamin Mostofi. 2022. Wiffract: a new foundation for RF imaging via edge tracing. In *Proceedings of the 28th Annual International Conference on Mobile Computing And Networking* (Sydney, NSW, Australia) *(MobiCom '22)*. Association for Computing Machinery, New York, NY, USA, 255–267. https://doi.org/10.1145/3495243.3514261

[35] William H Press. 2007. *Numerical recipes 3rd edition: The art of scientific computing*. Cambridge university press.

[36] Kun Qian, Zhaoyuan He, and Xinyu Zhang. 2020. 3D Point Cloud Generation with Millimeter-Wave Radar. *Proc. ACM Interact. Mob. Wearable Ubiquitous Technol.* 4, 4, Article 148 (dec 2020), 23 pages. https://doi.org/10.1145/3432221

[37] Yili Ren, Zi Wang, Yichao Wang, Sheng Tan, Yingying Chen, and Jie Yang. 2022. GoPose: 3D Human Pose Estimation Using WiFi. *Proc. ACM Interact. Mob. Wearable Ubiquitous Technol.* 6, 2, Article 69 (jul 2022), 25 pages. https://doi.org/10.1145/3534605

[38] Fei Shang, Panlong Yang, Yubo Yan, and Xiang-Yang Li. 2022. LiqRay: non-invasive and fine-grained liquid recognition system *(MobiCom '22)*. Association for Computing Machinery, New York, NY, USA, 296–309. https://doi.org/10.1145/3495243.3560540

[39] Fei Shang, Panlong Yang, Yubo Yan, and Xiang-Yang Li. 2023. PackquID: In-packet Liquid Identification Using RF Signals. *Proc. ACM Interact. Mob. Wearable Ubiquitous Technol.* 6, 4, Article 181 (jan 2023), 27 pages. https://doi.org/10.1145/3569469

[40] David M. Sheen, Douglas L. McMakin, and Thomas E. Hall. 2007. Near Field Imaging at Microwave and Millimeter Wave Frequencies. In *2007 IEEE/MTT-S International Microwave Symposium*. 1693–1696. https://doi.org/10.1109/MWSYM.2007.380033

[41] Hongbo Wang, Jingyang Hu, Tianyue Zheng, Jingzhi Hu, Zhe Chen, Hongbo Jiang, Yuanjin Zheng, and Jun Luo. 2024. MuKI-Fi: Multi-person Keystroke Inference with BFI-enabled Wi-Fi Sensing. *IEEE Transactions on Mobile Computing*

(2024), 1–15. https://doi.org/10.1109/TMC.2024.3368339

[42] Hao Wang, Daqing Zhang, Junyi Ma, Yasha Wang, Yuxiang Wang, Dan Wu, Tao Gu, and Bing Xie. 2016. Human Respiration Detection with Commodity Wifi Devices: Do User Location and Body Orientation Matter?. In *Proceedings of the 2016 ACM International Joint Conference on Pervasive and Ubiquitous Computing* (Heidelberg, Germany) *(UbiComp '16)*. Association for Computing Machinery, New York, NY, USA, 25–36. https://doi.org/10.1145/2971648.2971744

[43] Xuanzhi Wang, Kai Niu, Anlan Yu, Jie Xiong, Zhiyun Yao, Junzhe Wang, Wenwei Li, and Daqing Zhang. 2023. WiMeasure: Millimeter-level Object Size Measurement with Commodity WiFi Devices. 7, 2, Article 79 (jun 2023), 26 pages. https://doi.org/10.1145/3596250

[44] Xuyu Wang, Chao Yang, and Shiwen Mao. 2017. PhaseBeat: Exploiting CSI Phase Data for Vital Sign Monitoring with Commodity WiFi Devices. In *2017 IEEE 37th International Conference on Distributed Computing Systems (ICDCS)*. 1230–1239. https://doi.org/10.1109/ICDCS.2017.206

[45] Xuanzhi Wang, Anlan Yu, Kai Niu, Weiyan Shi, Junzhe Wang, Zhiyun Yao, Rahul C. Shah, Hong Lu, and Daqing Zhang. 2024. Understanding the Diffraction Model in Static Multipath-Rich Environments for WiFi Sensing System Design. *IEEE Transactions on Mobile Computing* (2024), 1–18. https://doi.org/10.1109/TMC.2024.3377708

[46] Claire M. Watts, Patrick Lancaster, Andreas Pedross-Engel, Joshua R. Smith, and Matthew S. Reynolds. 2016. 2D and 3D millimeter-wave synthetic aperture radar imaging on a PR2 platform. In *2016 IEEE/RSJ International Conference on Intelligent Robots and Systems (IROS)*. 4304–4310. https://doi.org/10.1109/IROS.2016.7759633

[47] Stephen J Wright. 2006. Numerical optimization.

[48] Chenhao Wu, Xuan Huang, Jun Huang, and Guoliang Xing. 2023. Enabling Ubiquitous WiFi Sensing with Beamforming Reports. In *Proceedings of the ACM SIGCOMM 2023 Conference* (New York, NY, USA) *(ACM SIGCOMM '23)*. Association for Computing Machinery, New York, NY, USA, 20–32. https://doi.org/10.1145/3603269.3604817

[49] Dan Wu, Ruiyang Gao, Youwei Zeng, Jinyi Liu, Leye Wang, Tao Gu, and Daqing Zhang. 2020. FingerDraw: Sub-Wavelength Level Finger Motion Tracking with WiFi Signals. *Proc. ACM Interact. Mob. Wearable Ubiquitous Technol.* 4, 1, Article 31 (March 2020), 27 pages. https://doi.org/10.1145/3380981

[50] Yaxiong Xie, Jie Xiong, Mo Li, and Kyle Jamieson. 2019. MD-Track: Leveraging Multi-Dimensionality for Passive Indoor Wi-Fi Tracking. In *The 25th Annual International Conference on Mobile Computing and Networking* (Los Cabos, Mexico) *(MobiCom '19)*. Association for Computing Machinery, New York, NY, USA, Article 8, 16 pages. https://doi.org/10.1145/3300061.3300133

[51] Zhiyun Yao, Xuanzhi Wang, Kai Niu, Rong Zheng, Junzhe Wang, and Daqing Zhang. 2024. WiProfile: Unlocking Diffraction Effects for Sub-Centimeter Target Profiling Using Commodity WiFi Devices. In *Proceedings of the 30th Annual International Conference on Mobile Computing and Networking* (<conf-loc>, <city>Washington D.C.</city>, <state>DC</state>, <country>USA</country>, </conf-loc>) *(ACM MobiCom '24)*. Association for Computing Machinery, New York, NY, USA, 185–199. https://doi.org/10.1145/3636534.3649355

[52] Enze Yi, Dan Wu, Jie Xiong, Fusang Zhang, Kai Niu, Wenwei Li, and Daqing Zhang. 2024. BFMSense: WiFi Sensing Using Beamforming Feedback Matrix. In *21st USENIX Symposium on Networked Systems Design and Implementation (NSDI 24)*. USENIX Association, Santa Clara, CA, 1697–1712. https://www.usenix.org/conference/nsdi24/presentation/yi

[53] L. Yujiri, M. Shoucri, and P. Moffa. 2003. Passive millimeter wave imaging. *IEEE Microwave Magazine* 4, 3 (2003), 39–50. https://doi.org/10.1109/MMW.2003.1237476

[54] Youwei Zeng, Dan Wu, Jie Xiong, Enze Yi, Ruiyang Gao, and Daqing Zhang. 2019. FarSense: Pushing the Range Limit of WiFi-Based Respiration Sensing with CSI Ratio of Two Antennas. *Proc. ACM Interact. Mob. Wearable Ubiquitous Technol.* 3, 3, Article 121 (Sept. 2019), 26 pages. https://doi.org/10.1145/3351279

[55] Xu Zewei, Peng Jieru, and Chen Xianqiao. 2015. A method for vehicle three-dimensional size measurement based on laser ranging. In *2015 International Conference on Transportation Information and Safety (ICTIS)*. 34–37. https://doi.org/10.1109/ICTIS.2015.7232075

[56] Fusang Zhang, Daqing Zhang, Jie Xiong, Hao Wang, Kai Niu, Beihong Jin, and Yuxiang Wang. 2018. From Fresnel Diffraction Model to Fine-Grained Human Respiration Sensing with Commodity Wi-Fi Devices. *Proc. ACM Interact. Mob. Wearable Ubiquitous Technol.* 2, 1, Article 53 (March 2018), 23 pages. https://doi.org/10.1145/3191785

[57] Yue Zheng, Yi Zhang, Kun Qian, Guidong Zhang, Yunhao Liu, Chenshu Wu, and Zheng Yang. 2019. Zero-Effort Cross-Domain Gesture Recognition with Wi-Fi. In *Proceedings of the 17th Annual International Conference on Mobile Systems, Applications, and Services* (Seoul, Republic of Korea) *(MobiSys '19)*. Association for Computing Machinery, New York, NY, USA, 313–325. https://doi.org/10.1145/3307334.3326081

[58] Yin Zhou and Oncel Tuzel. 2018. VoxelNet: End-to-End Learning for Point Cloud Based 3D Object Detection. In *2018 IEEE/CVF Conference on Computer Vision and Pattern Recognition*. 4490–4499. https://doi.org/10.1109/CVPR.2018.00472

[59] Vitaliy Zhurbenko (Ed.). 2011. *Electromagnetic Waves*. InTech.